ACS APPLIED ENERGY MATERIALS

www.acsaem.org Article

Impact of Fluorination on the Anodic Performance of Disodium Terephthalate: An Experimental and Computational Study

Daniel M. Harrison, Beenish Bashir, Eric Arkfeld, Andre Z. Clayborne,* and Chao Luo*

Cite This: https://doi.org/10.1021/acsaem.4c00664 Read Online

ACCESS | Metrics & More | Article Recommendations | Supporting Information

Downloaded via UNIV OF MIAMI on May 6, 2024 at 13:32:46 (UTC).
See https://pubs.acs.org/sharingguidelines for options on how to legitimately share published articles.

ABSTRACT: Advancing research into organic electrode materials is conducive for the development of affordable and sustainable Na-ion battery (NIB) technology owing to the low cost, abundance, and high structure tunability of organic materials. To obtain high-performance organic electrode materials, an in-depth understanding of the correlation between dynamic geometries of redox active functional groups in organic materials and electrochemical performance is critical but remains elusive. In this work, three fluorinated derivatives of disodium terephthalate (DTP) were synthesized to explore how fluorine substitutions altered the geometry and performance of the carboxylate groups in reversible sodiation/desodiation. Matching computational models, the monofluorinated disodium 2-fluoroterephthalate derivative outperformed disodium 2,3-difluoroterephthalate (196 mAh g^{-1} vs 88 mAh g^{-1}), and disodium tetrafluoroterephthalate was found to not be redox active. The difference in performance is attributed to the dynamic geometry caused by the fluorine substituents that disrupt the planarity of the molecules, preventing favorable redox reactions of the carboxylate functional groups. This effect is more pronounced with higher degrees of fluorination.

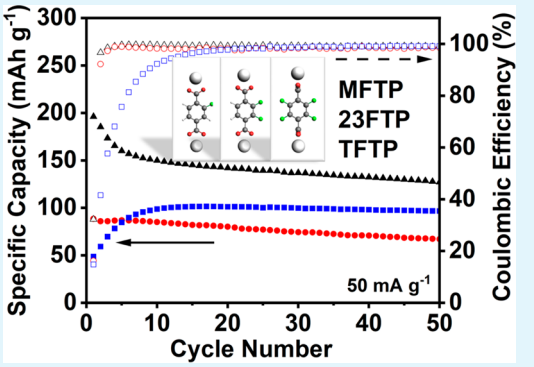

KEYWORDS: *Na-ion batteries, anode, fluorination, carboxylate, planarity, dynamic geometry*

INTRODUCTION

Global energy demands continue to grow, and advances in energy storage technologies are necessary to keep pace with this growth. While Li-ion batteries (LIBs) have succeeded as energy storage devices for portable electronics and electric vehicles due to high energy density and long cycle life, the scarcity and uneven distribution of the lithium and transition metal resources for LIBs result in high costs and low sustainability.[1] This compels research into alternative battery technologies beyond LIBs with low cost and high sustainability. Among various emerging battery systems, Na-ion batteries (NIBs) are considered as a promising alternative rechargeable battery technology, since sodium offers similar chemistry to lithium but is more abundant, cost-effective, and sustainable.[2] NIBs offer a wide array of applications in grid-scale energy storage, where cost and stability are much more important than energy density. However, the high-performance electrode materials in LIBs do not extend their performance to those in NIBs. For example, the lower binding energy and larger ionic radius of Na^+ ions results in poor intercalation chemistry in graphite, which is the most common anode in LIBs.[3−6] Sodium metal anodes, analogous to lithium metal anodes, suffer from dendrite formation and poor cyclability due to parasitic reactions with the electrolyte.[7] Hard carbon functions as a usable alternative for Na^+ intercalation but brings its own challenges. Primarily, hard carbon requires discharge to near 0 V to fully realize its capacity, and at such low potentials, plating of sodium metal at the interfacial surface of the electrode is induced, promoting dendrite formation that leads to battery short circuit.[8−10] Additionally, the production of hard carbon is time- and energy-consuming.[11] This necessitates research into alternative materials with low cost and low redox potentials.

Among various anode materials in NIBs, organic materials are promising because of their abundance, affordability, high structure tunability, and abundant structural diversity.[12,13] So far, five categories of organic functional groups have been identified as redox active centers in NIBs: carbonyl, imine, azo, thioketone, and amine groups.[14−18] Carbonyl groups in carboxylates and esters have received substantial attention for organic anode materials (OAMs) owing to their low redox potentials (<1 V versus Na/Na^+).[19] Additionally, carboxylic acids can easily be "salted out" through simple neutralization reactions with sodium bases, which increase the polarity of the molecules, modify the redox activity, and reduce the solubility

Received: March 14, 2024
Revised: April 8, 2024
Accepted: April 10, 2024

© XXXX American Chemical Society

in the electrolytes.[20] Research on the chemical modification of OAMs has mostly focused on extending conjugation or installing electron donating/withdrawing groups to optimize the electrochemical performances.[21] Fluorination is a unique chemical modification method to tune the electrochemical behavior of organic molecules. Compared to the bulkiness of other electron-withdrawing groups, such as nitro or carbonyl groups, the extreme electronegativity and small size of the fluorine atom offers unique electron-withdrawing behavior.[22] This small size also leads to orbital overlap with aryl carbons that helps stabilize resonance structures, which has been shown to improve the reversibility of the anodic redox reaction.[23] However, there has been a lack of research on the impact of chemical modification on the macroscale properties of bulk molecular structures in relation to the redox performance in active materials. Computational studies have supported these research efforts by exploring the highest occupied molecular orbital (HOMO)-lowest unoccupied molecular orbital (LUMO) energy gaps of these variations.[24] However, experimental and computational studies into the dynamic geometry between the ground state and reduced anode species have not been deeply explored and can reveal new directions in the tuning of the OAMs.

Our previous work showed that fluorines *ortho* to aryl sodium carboxylate salts showed better capacity and cycling stability than chlorine and bromine analogues, as well as the nonhalogenated sodium terephthalate.[25] The fluorine atom in the fluorinated carboxylate can interact weakly with inserted Na^+ by an ion-dipole interaction upon cycling, which improves the cyclic stability. In addition, the atomic weight of fluorine is lower than that of chlorine and bromine, resulting in higher specific capacity of the fluorinated carboxylate than the other halogenated carboxylates. To further explore how position and degree of fluorination affects the electrochemical performance of disodium terephthalate salts, three compounds were synthesized and tested, that is, disodium 2-fluoroterephthalate (MFTP), disodium 2,3-difluoroterephthalate (23FTP), and disodium tetrafluoroterephthalate (TFTP). Additionally, computational studies of the three compounds, along with other analogues, were conducted to determine thermodynamic and geometric behaviors of the dicarboxylates during first and second sodiation/desodiation. Of the three organic salts tested, MFTP showed the best performance, matching the computational predictions due to geometric arrangement. Compared with the other anode materials such as Na metal, hard carbon, etc., the fluorinated carboxylates have the advantages of low cost, abundance, high sustainability, and high structure tunability. The fluorinated carboxylate anodes are dendrite-free upon cycling since their redox potentials are at ~0.4 V, and they can be synthesized in ethanol at room temperature, which is facile and energy-efficient. More importantly, the molecular structure of fluorinated carboxylates can be easily tailored by manipulating the functional groups, conjugation structures, structure isomerism, and dynamic geometry, offer opportunities for optimizing their performances in NIBs.

EXPERIMENTAL SECTION

Material Synthesis. 3-Fluoro-4-methyl-benzoic acid and tetrafluoroterephthalic acid (TFTA) were purchased from TCI America; 2, 3-difluoro-4-methyl-benzoic acid was purchased from Combi Blocks. The oxidation of 3-fluoro-4-methyl-benzoic acid and 2, 3-difluoro-4-methyl-benzoic acid were carried out by first dissolving in a 5% (w/w) KOH aqueous solution, then a 5:1 stoichiometric ratio of $KMnO_4$ was added, and the solution was refluxed for 24 h. The solution was filtered, centrifuged, and decanted to remove insoluble MnO_2, and then 12 M HCl was added dropwise to precipitate out the product and collected by filtration. The acids were washed with DI water and dried under vacuum at 100 °C overnight. The resulting products, monofluoroterepthalic acid (MFTA) and 2,3-difluoroterephthalic acid (OFTA), were both white powders. Sodiation was achieved by dispersing the acids (MFTA, OFTA, and TFTA) in pure ethanol with sodium hydroxide in a 5% stoichiometric excess and stirred overnight. The products (MFTP-Na, 23FTP-Na, and TFTP-Na) were filtered and rinsed with pure ethanol three times and dried under vacuum at 150 °C overnight. Each organic salt was a white powder.

Material Characterizations. XRD pattern was recorded by a Rigaku MiniFlex 600 system using CuKα radiation; Raman measurements were performed on a Horiba Jobin Yvon Labram Aramis instrument using a 532 nm diode-pumped solid-state laser, attenuated to give ~900 μW power at the sample surface; FTIR was recorded by an Agilent Cary 630 FTIR instrument; SEM images were taken by a JEOL JSM-IT500HR InTouchScope SEM instrument (Japan); NMR tests were performed with a Bruker Ascend 400 NMR spectrometer. MS tests were performed with a Sciex QTRAP 4500. Samples were prepared at a concentration of 1 μg mL^{-1} in water and directly infused into a mass spectrometer.

Electrochemical Measurements. Electrodes were prepared with each terephthalate salt by mixing with carbon black (CB) and Polyvinylidene fluoride (PVDF) in a mass ratio of 6:3:1, dispersing in *N*-methyl-2-pyrrolidine (NMP) to form a slurry, and casting onto copper foil via a doctor blade at 200 nm thickness and drying at 80 °C overnight and then 24 h under vacuum at 100 °C. The coated foil was punched into round electrodes (diameter 1.11 cm) and possessed an average mass loading of 1.5−2.0 mg. Coin cells were assembled with sodium metal as the counter electrode, varied concentrations of $NaPF_6$ in diethylene glycol dimethyl ether (DEGDME) electrolyte, with glass fiber separators. Electrochemical performance tests were carried out on an Arbin battery test station (LBT20084, Arbin Instruments, USA). Cyclic voltammograms and impedance tests were conducted on a Gamry Interface 1010 E Potentiostat/Galvanostat/ZRA. A current density of 50 mA g^{-1} was used in the galvanostatic intermittent titration test (GITT) test, applied during the charge or discharge for 30 min, and then the cell rested for 3 h. For postcycling X-ray diffraction (XRD) and Fourier transform infrared spectroscopy (FTIR) characterization, high mass loading electrodes were used. The composite was made with polytetrafluoroethylene (PTFE) binder in a mass ratio of 8:1:1 with CB to decrease the signal of CB.

Theoretical capacity values for MFTP-Na, 23FTP-Na, and TFTP-Na were calculated with the formula:

$$C = [n^*F]/M$$

where n is the number of electrons transferred, F is Faraday's Constant, and M is the molar mass of the compound. All three salts are expected to undergo a two-electron reaction. Based on the molar mass of each salt, MFTP-Na C_{th} = 235.01 mAh g^{-1}; OFTP-Na C_{th} = 217.82 mAh g^{-1}; and TFTP-Na C_{th} = 190.04 mAh g^{-1}.

Theoretical Calculation Details. Density functional theory (DFT) calculations were executed by the Gaussian 16 program with the B3LYP/6-311+G* level of theory.[26−30] The Grimme-D3 scheme was used to include van der Waals interactions between atoms.[31,32] The molecular geometry optimizations were performed using the lowest possible spin state, singlet or doublet, and spin polarization. Single point frequency analyses ensured the absence of negative frequencies and the ground state of the structure geometry.

Utilizing the results from frequency analysis, statistical thermal corrections were applied, wherein the Gibbs energy (G) for each optimized geometry was calculated using the formula:

$$G = E_{DFT} + ZPE - TS \quad (1)$$

where E_{DFT}, ZPE, T, and S represent DFT energy, zero-point energy, temperature (298.15 K), and entropy, respectively. The calculated Gibbs energy was used to identify the lowest energy structures of

https://doi.org/10.1021/acsaem.4c00664
ACS Appl. Energy Mater. XXXX, XXX, XXX−XXX

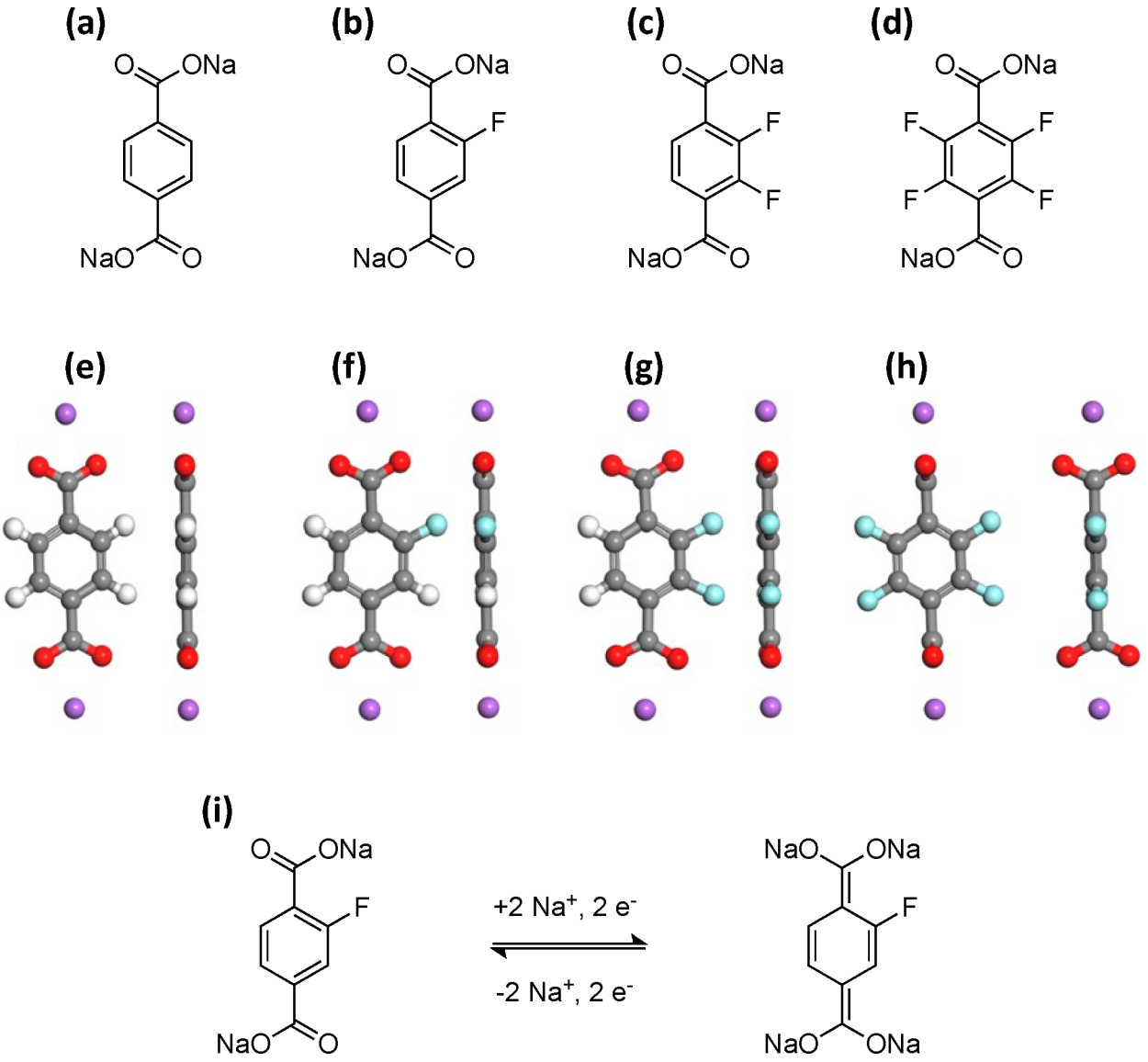

Figure 1. Molecular structures of (a) DTP, (b) MFTP, (c) 23FTP, and (d) TFTP. Ground state geometries, front (left) and side (right), of (e) DTP, (f) MFTP, (g) 23FTP, and (h) TFTP. The C, H, O, F, and Na atoms are represented by gray, white, red, cyan, and purple ball colors, respectively. (i) Redox reaction mechanism of MFTP.

MFTP and 23FTP molecules tested for a given state. For structures having adsorbed sodium atoms, the Gibbs free energy of a single sodium was approximated as 1/2 that of the optimized dimer (G_{Na_2} at the same level of theory. Utilizing the minimum energy configurations for each adsorption, the change in Gibbs free energy of adsorption (ΔG) was calculated in a stepwise fashion according to

$$\Delta G = G_n - G_{n-1} - \frac{1}{2}G_{Na_2} \quad (2)$$

where n, G_n and G_{n-1} represent the number of adsorbed Na atoms and the Gibbs free energies of the optimized molecules with n and $n-1$ adsorbed Na atoms, respectively. Binding energies (ΔE) were calculated for each adsorption step according to

$$\Delta E = E_n - E_{n-1} - \frac{1}{2}E_{Na_2} \quad (3)$$

where E_{Na_2}, E_n, and E_{n-1} are the DFT Energies of the optimized Na-dimer and the minimum energy configurations with n and $n-1$ adsorbed Na atoms.

RESULTS AND DISCUSSION

The ground state configurations of the fluorinated disodium terephthalate (DTP) structures are shown in Figure 1. Fluorination of the molecule marginally affected the six-membered carbon ring of the molecule while notably changing the carboxylate groups orientation with fluorine atoms rising to four. This effect is exemplified in TFTP, where the carboxylate groups are oriented at 90°. This torsion is attributed to electrostatic repulsion between the carboxylate groups and fluorine atoms. At the same time, the electron-withdrawing effects of the fluorine reduced charge delocalization in the six-membered carbon ring. The studied fluorinated DTP molecular systems indicate negligible differences in their bond lengths (Figure S1).

We investigated the electronic structure, the HOMO and LUMO levels of each molecule, to gain insight into the possible performance as an anode material. Addition of fluorine atoms induced significant changes in the HOMOs and LUMOs of the DTP molecules, as shown in Figure 2. For

https://doi.org/10.1021/acsaem.4c00664
ACS Appl. Energy Mater. XXXX, XXX, XXX−XXX

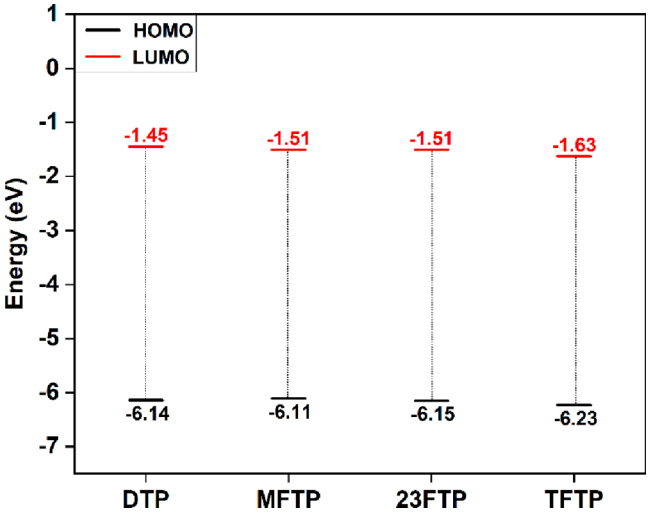

Figure 2. HOMO and LUMO energies of the DTP, MFTP, 23FTP, and TFTP molecular systems.

instance, the HOMO energy increased for MFTP (0.03 eV) but decreased for 23FTP (−0.01 eV) and TFTP (−0.08 eV) compared to DTP. In addition, all the LUMO energies of MFTP (−0.06 eV), 23FTP (−0.06 eV), and TFTP (−0.16 eV) were reduced compared to DTP.

Furthermore, the number of fluorine atoms and their position on the carbon ring significantly influenced the spatial distribution of HOMO and LUMO (Figure S2). The electron densities of HOMOs were found to be predominantly concentrated on the six-membered carbon ring and the fluorine atoms in the DTP, MFTP, and 23FTP molecular systems. The coupled π-orbitals in the carbon ring facilitated the π-electrons delocalization and maintained the planar conformation throughout the molecule. However, the HOMOs extended between the six-membered carbon ring and carboxylate groups in the TFTP system. The steric hindrance between carboxylate groups and fluorine atoms may not allow planar conformation in the TFTP system, undermining the probable relationship between the TFTP structure and orbitals symmetry. Besides, the LUMOs were primarily localized on the oxygen(s) and sodium(s) of the carboxylate groups in all of the structures. This electron density distribution in the fluorinated DTP structures exhibits harmonious patterns with changing number of fluorine atoms, promoting a significant gap in the HOMO, LUMO, and HOMO−LUMO gap energies (Table S1).

As reported before, the narrow gap between HOMO−LUMO energies suggests superior battery performance,[32] and accordingly MFTP is supposed to perform better. Additionally, the electrochemical performance of these systems is found to be dependent on the spatial distribution of HOMO and LUMO. We also compared 23FTP with a previously synthesized 25FTP system and simulated 26FTP to better understand the role of fluorine atoms position in the electronic structure.[25] The fluorine position did not affect the planar geometries and bond lengths in the studied systems, resulting in nearly similar electronic cloud distribution (Figure S3). Still, the position of fluorine atoms in the molecular framework of 23FTP, 25FTP, and 26FTP systems significantly influenced their HOMO and LUMO energy levels. We investigated the interactions between the first and second sodium atoms adsorbed onto each molecule to explore the reaction mechanism underlying the MFTP's superior performance over 23FTP in NIBs (Figure 3). The adsorption of the first

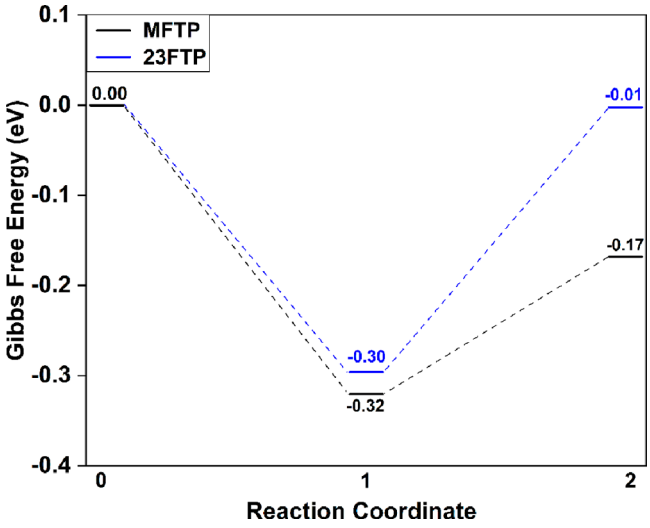

Figure 3. Free energy diagram for consecutive Na adsorptions on MFTP (black) and 23FTP (blue). Note that the reaction coordinate denotes the number of adsorbed sodium atoms.

sodium atom was favorable for both the MFTP and 23FTP systems, indicated by the negative ΔG values. However, the second sodium atom faced steric hindrance in 23FTP due to a nonplanar conformation (carboxylate torsion angle: 170°) compared to planar structure of MFTP (carboxylate torsion angle: 180°), as shown in Figure S4. The planar geometry of MFTP offers a distinct advantage. It enhances structural stability by promoting a uniform distribution of strain across the molecule. This, in turn, facilitates electron transfer between the adsorbed sodium ions and the MFTP framework, leading to faster reaction kinetics and improved cyclic stability compared to the nonplanar 23FTP.[33] Consequently, MFTP with a planar conformity can perform better as an organic anode material in NIBs than 23FTP.

With an understanding of the HOMO/LUMO energy and spatial structures of DTP and its derivatives, we further performed the synthesis and characterization of MFTP, 23FTP, and TFTP to determine their performance as anodes. The chemical structures of the three fluorinated terephthalate salts were characterized by various methods such as X-ray diffraction (XRD), nuclear magnetic resonance (NMR), Fourier transform infrared spectroscopy (FTIR), Raman spectroscopy, scanning electron microscopy (SEM), and mass spectrometry (MS). Figure 4a and S5a,b show XRD patterns of MFTP, 23FTP, and TFTP. There are unique diffractions for each salt, showing different crystalline structures. NMR was utilized to further confirm the organic salt structures. Deuterium oxide (D_2O) was used as the solvent (HOD signal at 4.8 ppm). The ^{1}H NMR for MFTP (Figure 4b) shows a tightly grouped unsymmetric quintet (7.461, 7.490, 7.516, 7.547, and 7.566 ppm), arising from a triplet overlapping with two doublets due to the extended coupling observed in aryl rings. The hydrogen on C5 couples with both the hydrogen on C3 and on C6 to produce a triplet, while the other two hydrogens each produce a doublet signal. The ^{13}C NMR spectrum for MFTP-Na (Figure 4c) shows nine signals. The compound contains eight unique carbon environments, the ninth peak arises from spin−spin coupling with fluorine.

https://doi.org/10.1021/acsaem.4c00664
ACS Appl. Energy Mater. XXXX, XXX, XXX−XXX

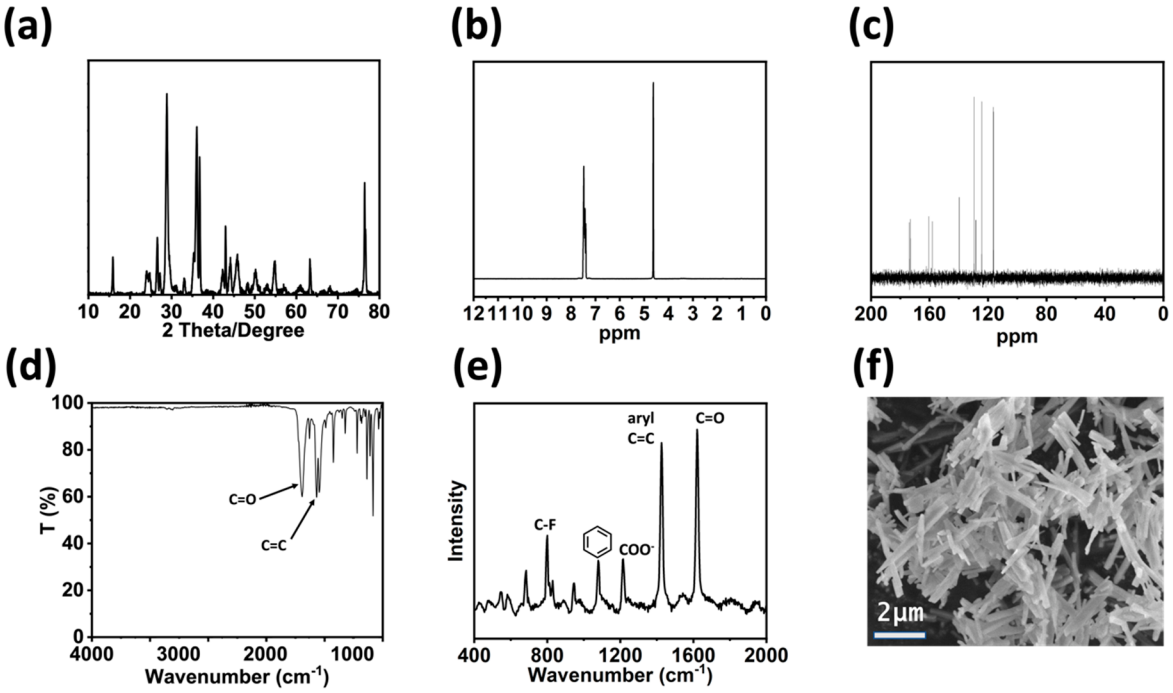

Figure 4. Characterization of MFTP. (a) XRD pattern, (b) ^{1}H NMR spectrum, (c) ^{13}C NMR spectrum, (d) FTIR spectrum, (e) Raman spectrum, and (f) SEM image.

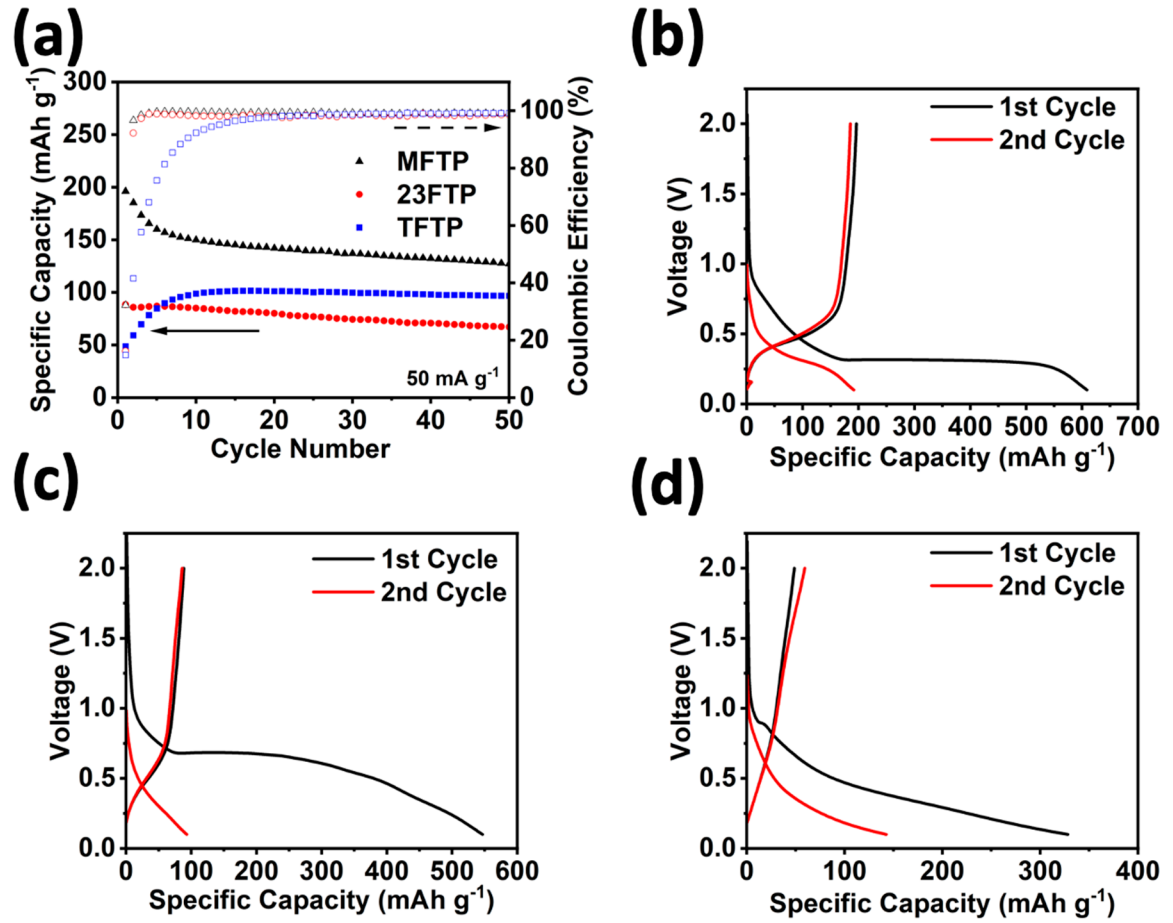

Figure 5. Electrochemical performances of MFTP, 23FTP, and TFTP. (a) Cycle life and Coulombic efficiency (CE) overlay of each salt at 50 mA g^{-1}, (b) galvanostatic charge−discharge curves for 1st and 2nd cycle of MFTP at 50 mA g^{-1}, (c) galvanostatic charge−discharge curve for 1st and 2nd cycle of 23FTP at 50 mA g^{-1}, (d) galvanostatic charge−discharge curve for 1st and 2nd cycle of TFTP at 50 mA g^{-1}.

https://doi.org/10.1021/acsaem.4c00664
ACS Appl. Energy Mater. XXXX, XXX, XXX−XXX

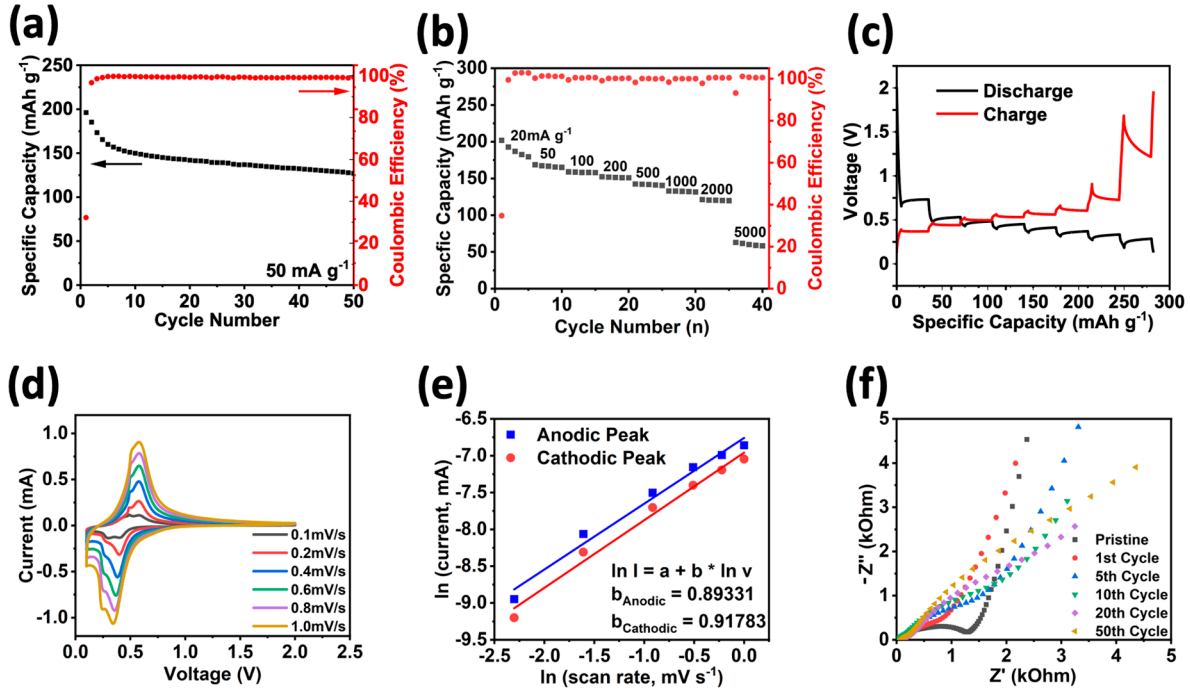

Figure 6. Electrochemical performance of MFTP. (a) Cycle life and CE at 50 mA g^{-1}, (b) rate capability test at various current densities, (c) GITT test at a current density of 50 mA g^{-1}, (d) CV curves at various scan rates from 0.1 to 1.0 mV s^{-1}, (e) relationship of the natural logarithm of scan rates and corresponding peak currents, and (f) EIS tests of the pristine cell and electrodes after specific cycles.

The full structure is confirmed by Attached Proton Test C-13 NMR (APT-CNMR) with J-coupling analysis, as shown in Figure S6. The ^{1}H spectrum of 23FTP is shown in Figure S5c and presents only one signal at 7.273 ppm because both hydrogens on the ring share the same chemical environment. The ^{13}C spectrum (Figure S5e) for 23FTP gives a signal at 171.60 ppm for the sp^2 carboxylate carbons, a doublet of doublets at 149.37, 149.20, 146.86, and 146.70 ppm that represents the benzyl carbons bonded to fluorine, confirmed by APT CNMR and J-Coupling Analysis (Figure S7). Fluorine also couples to the benzyl carbons bonded to hydrogen on the opposite side of the ring, producing a triplet at 123.8 ppm, and the carbons bonded to the carbonyl group produce a doublet at 123.82 ppm. TFTP-Na does not display any signal in its ^{1}H spectrum except for the solvent peak (Figure S 5d). The ^{13}C shows a signal at 166.02 ppm for the carbonyl carbon, and three signals with complex splitting patterns around 143.4, 140.9, and 118.7 ppm for the aryl carbons bonded to fluorine and to the carbonyl carbon (Figure S 5f). The NMR spectra support that each salt was synthesized and sodiated successfully. FTIR was also employed to confirm the successful synthesis. All three compounds display a strong absorbance for the asymmetric carboxylate stretch (MFTP: 1578 cm^{-1} (Figure 4d); 23FTP: 1580 cm^{-1} (Figure S8a); TFTP: 1602 cm^{-1} (Figure S8b)), and symmetric carboxylate vibrational stretch (MFTP: 1410 and 1379 cm^{-1}; 23FTP: 1396 cm^{-1}; TFTP: 1390 cm^{-1}). MFTP displays a split carbonyl peak due to the orthofluoro group adjacent to only one of the carboxylate groups. Absorbances for the C−F bond appear at 1219, 1248, and 982 cm^{-1}, for MFTP, 23FTP, and TFTP respectively. MFTP also shows a characteristic triple peak at 831, 796, and 760 cm^{-1} representing a trisubstituted aryl ring. Lastly, given the generally strong absorbance of carboxylic acid O−H signals, the absence of any such peak further shows the successful deprotonation and sodiation of the terephthalate salts. Raman spectroscopy was also performed on each salt, showing expected carboxylate peaks. Figure 4e shows the Raman spectrum for MFTP, displaying a carbonyl peak at 1622 cm^{-1}, an aryl C═C peak at 1425 cm^{-1}, a carboxylate anion peak at 1212 cm^{-1}, an aryl ring absorption peak at 1081 cm^{-1}, and a C−F bond peak at 797 cm^{-1}. Figure S8c and S8d show similar carbonyl, aryl C═C, and C−F peaks for 23FTP at 1625, 1316, and 735 cm^{-1}, and similarly for TFTP at 1649, 1382, and 511 cm^{-1}, respectively. SEM imaging of the three salts shows unique morphologies. MFTP (Figure 4f) particles are rod-like in shape with an average length of 1−2 um and thickness of around 200 nm. 23FTP (Figure S8e) shows tighter packing of particles that are flat in shape and wider than MFTP, but similar length and thickness. TFTP (Figure S8f) shows a much denser packing with larger particle sizes. The larger surface area of MFTP increases electrochemical kinetics and contribute to the better cycling performance out of the three salts. Mass spectrometry (MS) of the salts show molecular ion peaks of 227.98, 245.97, and 281.95 m/z (Figures S9−11) for MFTP, 23FTP, and TFTP, respectively, matching well with calculated molecular weights. The initial fragmentation peak for each compound shows a loss of 46 m/z, representing the loss of two sodium atoms. Further fragmentation for each compound shows a loss of 44 m/z, representing the loss of a carboxylate group. The MS data further confirms correct synthesis. Therefore, these results confirm the chemical structures and morphology of MFTP, 23FTP, and TFTP.

Electrochemical Performance. Electrochemical performance of each salt was conducted in a half-cell using sodium metal as the counter electrode. Initial testing utilized a 1 M $NaPF_6$ in a DEGDME electrolyte system to gauge the performance of each organic salt at a current density of 50 mA g^{-1}. Figure 5a shows MFTP with an initial capacity of 196 mAh g^{-1}, which is much higher than the initial capacities of

https://doi.org/10.1021/acsaem.4c00664
ACS Appl. Energy Mater. XXXX, XXX, XXX−XXX

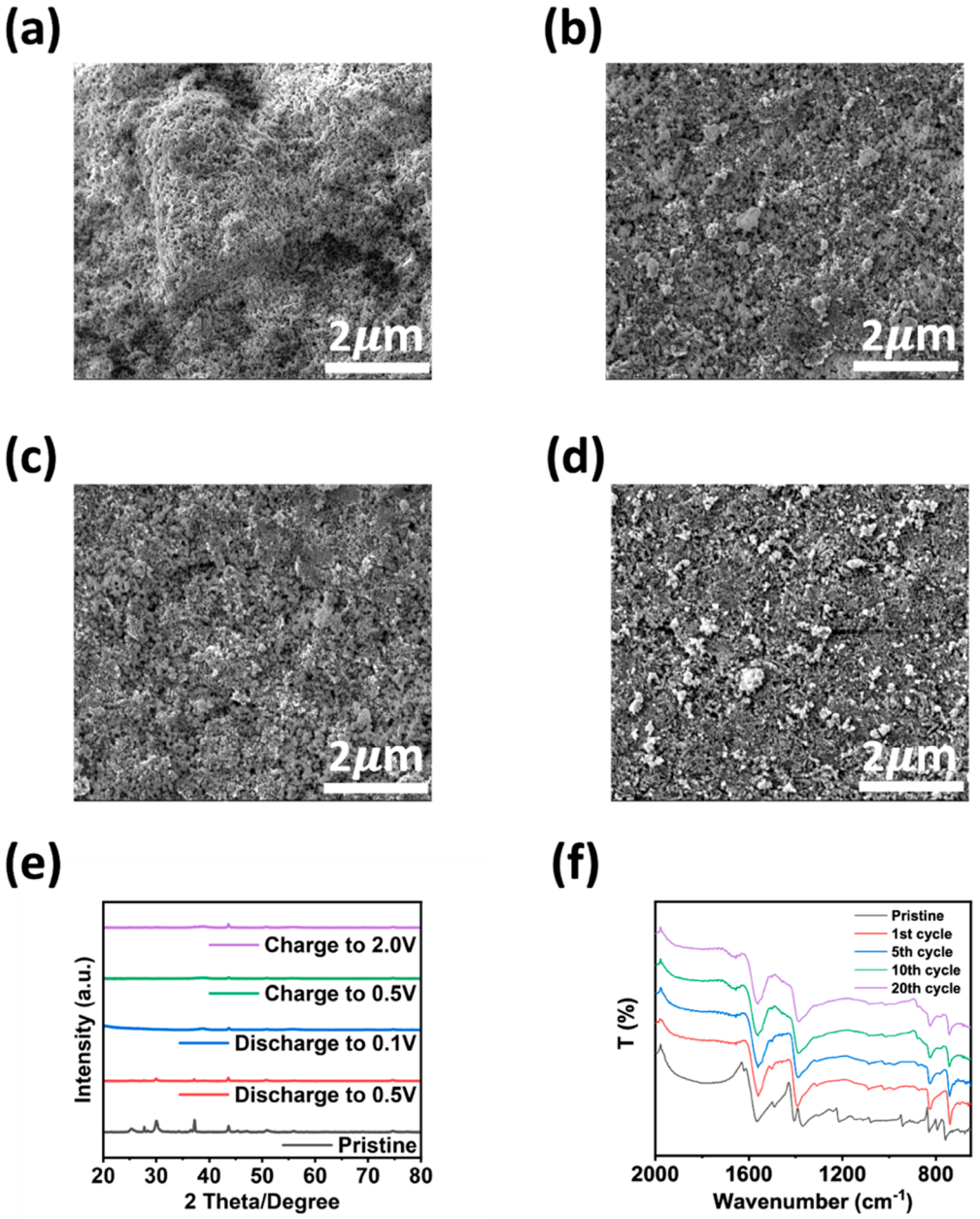

Figure 7. Postcycling characterization of MFTP electrodes. (a-d) SEM images of pristine, after 1 cycle, after 5 cycles, and after 10 cycles, (e) XRD patterns of electrodes discharged or charged to various potentials within a cycle, and (f) FTIR spectra before and after cycling.

23FTP (88 mAh g^{-1}) and TFTP (48 mAh g^{-1}). The high reversible capacity of MFTP is retained for 50 cycles, representing the best performance among the three anode materials. The Galvanostatic charge/discharge curves show redox plateaus around 0.4 V for both MFTP and 23FTP (Figure 5b,c). However, TFTP did not show any plateaus on charge or discharge (Figure 5d). The galvanostatic charge/discharge curves at fifth, 10th, 20th, and 50th cycles for MFTP, 23FTP, and TFTP are also shown in Figure S12. To further confirm the lack of redox activity in TFTP, CB electrodes (9:1 ratio with PVDF binder) were cycled under the same conditions (Figure S13). The initial capacity of CB (111 mAh g^{-1}) was higher than TFTP, and the galvanostatic charge and discharge curves presented the same shape, indicating that TFTP was not electrochemically active and hindered the capacity of the CB in the electrode. This supports the computational determination of the out-of-plane torsioned carboxylate groups of TFTP preventing resonance contributions for sodiation and desodiation. There is 60 wt % TFTP in the electrode, which is not only electrochemically inactive but also has low electronic conductivity. It reduces the reaction kinetics and results in an activation process for carbon black to fully react with Na^+, so the capacity of the TFTP electrode increases in the initial cycles.

With MFTP showing the best performance, further testing was conducted. High and low concentration electrolyte systems were employed to explore cycling optimization. The overlay in Figure S14 shows that both 1 and 2 M $NaPF_6$ in DEGDME electrolytes yield similar initial capacity of 196 mAh g^{-1}. After initial cycling (<10 cycles), the battery with 2 M $NaPF_6$ in DEGDME electrolyte showed a slightly lower capacity than that with 1 M $NaPF_6$ in DEGDME electrolyte, but also lower capacity fading upon long-term cycling. The battery with an ultralow 0.1 M $NaPF_6$ in DEGDME electrolyte

https://doi.org/10.1021/acsaem.4c00664
ACS Appl. Energy Mater. XXXX, XXX, XXX−XXX

displayed lower capacity than that with 1M/2 M $NaPF_6$ in DEGDME electrolytes. These results demonstrate that the battery with 2 M $NaPF_6$ in DEGDME electrolyte showed the best cyclic stability; therefore, it was selected for all subsequent testing.

The cycling performance of MFTP with 2 M $NaPF_6$ in the DEGDME electrolyte is shown in Figure 6a. The initial capacity is 195.31 mAh g^{-1}. The rate capability test in Figure 6b shows cycling from an increasing current density of 20 mA g^{-1} to 5A g^{-1}, and the corresponding specific capacity falling from an initial 202 mAh g^{-1} to 58 mAh g^{-1}. GITT (Figure 6c) was employed to determine the overpotentials of MFTP. The charge and discharge potentials at 0.6 and 0.4 V, respectively, show associated overpotentials of 23 and 29 mV. These low overpotentials suggest fast reaction kinetics, matching the predicted performance of the monofluorinated salt. Using cyclic voltammetry (CV), MFTP was scanned from 0.1 to 1.0 mV s^{-1} (Figure 6d) to further understand the kinetic behavior. The natural log of the peak currents at each scan rate was plotted against the natural log of the scan rate in Figure 6e. The slopes of the linear fit of both the cathodic and anodic peaks (0.9178 and 0.8933, respectively) are close to a value of 1, showing that the kinetic behavior of the material is controlled by the surface reaction. The interfacial resistance of the MFTP electrode was studied by electrochemical impedance spectroscopy (EIS). The pristine anode shows a high initial resistance of 1294 Ω for the depressed semicircle (Figure 6f), which is significantly decreased upon cycling. This suggests a change in the interface between the anode and the electrolyte that facilitates charge transfer. Additionally, the low-frequency Warburg tail region indicates ion diffusion behavior. The typical slope of 45° assumes a uniform planar surface for ions to diffuse through.[34] Steeper slopes indicate additional modes for capacitance beyond diffusion, such as porosity. As cycling occurs, the slope of the Warburg tail decreases, showing a loss of porosity in the electrode composite, and as the slope falls below 45°, suggests that ion diffusion is also disrupted.[35]

Postcycling characterization of the electrode was conducted with SEM, XRD, and FTIR to reveal the crystalline and morphological changes that the electrode undergoes during cycling. Figure 7a shows SEM images of the pristine electrode, and Figure 7b-d shows cycled electrodes. After cycling, the surface morphology becomes less uniform. This matches well with the slow capacity fading of the anode. Figure 7e shows XRD of the anode at different potentials within one discharge/charge cycle. While some peaks remain throughout cycling, many peaks in the pristine electrode do not recover after charging, demonstrating the phase change after first cycle. With SEM and XRD showing changes in the bulk electrode material, FTIR was also employed on cycled electrodes to investigate if there were chemical bond changes over cycling. As shown in Figure 7f, the spectra of cycled electrodes exhibit obvious peak changes at 790, 1211, and 1362 cm^{-1} after cycling. This supports that the loss in the capacity of MFTP cells is due to structural changes occurring during cycling. Further structure optimization is necessary to stabilize MFTP upon long-term cycling in the NIBs.

CONCLUSION

The monofluorinated MFTP electrochemically outperforms the 23FTP and TFTP in NIBs. The higher degrees of fluorination lead to a disruption of the planarity of the dicarboxylate compounds, hindering the redox reactivity. This effect is more pronounced when the fluorine substituents are in close proximity to each other. Through computational modeling, TFTP was shown to display a 90° rotation of the carboxylate group, preventing redox reactivity, and thus not being electrochemically active. While fluorine substitution did not affect bond lengths, fluorination was found to alter HOMO−LUMO gaps as well as charge distribution, and experimental performance was well predicted from the *in-silico* modeling. MFTP displayed a high initial capacity of 196 mAh g^{-1}, slow capacity decay, and high rate capability up to 5A g^{-1} in NIBs, while 23FTP and TFTP exhibit much lower capacity and low redox activity. These results elaborate on the influence of fluorination on aryl carboxylate salts in NIBs. Fluorines ortho to aryl carboxylate groups allow for narrower HOMO−LUMO gaps and influence charge distribution, leading to improved capacity and reversibility. However, two fluorines surrounding a carboxylate group rotate the redox active functional group out of plane, disrupting the resonance contribution and therefore inhibiting a redox reaction. Additionally, 23FTP shows that the adjacent fluorines lower redox activity. These findings allow for the improved rational design of future high-performance organic anode materials for NIBs.

ASSOCIATED CONTENT

Supporting Information

The Supporting Information is available free of charge at https://pubs.acs.org/doi/10.1021/acsaem.4c00664.

The front and side views of DTP, MFTP, 23FTP, TFTP (Figure S1); Spatial orbital distribution of HOMO and LUMO of DTP, MFTP, 23FTP, TFTP (Figure S2); The front and side views and spatial orbital distribution of HOMO and LUMO of 23FTP and 25 FTP (Figure S3); The predicted sodiation structures of MFTP and 23FTP (Figure S4); Material Characterization for 23FTP and TFTP (Figure S5); 13C NMR spectrum of MFTP (Figure S6); 13C NMR spectrum of 23FTP (Figure S7); Characterization of 23FTP and TFTP (Figure S8); Mass spectrum of MFTP (Figure S9); Mass spectrum of 23FTP (Figure S10); Mass spectrum of 23FTP (Figure S11); Cycling performances of TFTP and CB (Figure S12); Galvanostatic charge/discharge curves of MFTP, 23FTP, and TFTP up to 50 cycles (Figure S13); Cycling Performance comparison of MFTP in various electrolytes (Figure S14); The front and side views and spatial orbital distribution of HOMO and LUMO of Tri FTP (Figure S15); Calculated HOMO, LUMO, and Gap Energies for DTP, MFTP, 23FTP, and TFTP (Table S1) (PDF)

AUTHOR INFORMATION

Corresponding Authors

Chao Luo − *Department of Chemistry and Biochemistry, George Mason University, Fairfax, Virginia 22030, United States; Department of Chemical, Environmental, and Materials Engineering, University of Miami, Coral Gables, Florida 33146, United States;* orcid.org/0000-0001-8497-8548; Email: cxl1763@miami.edu

Andre Z. Clayborne − *Department of Chemistry and Biochemistry, George Mason University, Fairfax, Virginia 22030, United States*; Email: aclaybo@gmu.edu

https://doi.org/10.1021/acsaem.4c00664
ACS Appl. Energy Mater. XXXX, XXX, XXX−XXX

Authors

Daniel M. Harrison − *Department of Chemistry and Biochemistry, George Mason University, Fairfax, Virginia 22030, United States*

Beenish Bashir − *Department of Chemistry and Biochemistry, George Mason University, Fairfax, Virginia 22030, United States*

Eric Arkfeld − *Department of Chemistry and Biochemistry, George Mason University, Fairfax, Virginia 22030, United States*

Complete contact information is available at: https://pubs.acs.org/10.1021/acsaem.4c00664

Notes

The authors declare no competing financial interest.

■ ACKNOWLEDGMENTS

This work was supported by the US National Science Foundation Award No. 2154145. The authors also acknowledge the support from the Quantum Science & Engineering Center and College of Science at George Mason University. We are thankful for the technical support for mass spectroscopy from Dr. Michael Girgis and Dr. Mikell Paige from the Center of Molecular Engineering at George Mason University.

■ REFERENCES

(1) Chen, X.; Zhang, Y. The main problems and solutions in practical application of anode materials for sodium ion batteries and the latest research progress. *International Journal of Energy Research* **2021**, *45* (7), 9753−9779.

(2) Tan, H.; Chen, D.; Rui, X.; Yu, Y. Peering into alloy anodes for sodium-ion batteries: current trends, challenges, and opportunities. *Adv. Funct. Mater.* **2019**, *29* (14), 1808745.

(3) Perveen, T.; Siddiq, M.; Shahzad, N.; Ihsan, R.; Ahmad, A.; Shahzad, M. I. Prospects in anode materials for sodium ion batteries-A review. *Renewable and Sustainable Energy Reviews* **2020**, *119*, 109549.

(4) Xu, Z.-L.; Yoon, G.; Park, K.-Y.; Park, H.; Tamwattana, O.; Joo Kim, S.; Seong, W. M.; Kang, K. Tailoring sodium intercalation in graphite for high energy and power sodium ion batteries. *Nat. Commun.* **2019**, *10* (1), 2598.

(5) Kim, H.; Hong, J.; Yoon, G.; Kim, H.; Park, K.-Y.; Park, M.-S.; Yoon, W.-S.; Kang, K. Sodium intercalation chemistry in graphite. *Energy Environ. Sci.* **2015**, *8* (10), 2963−2969.

(6) Park, J.; Xu, Z.-L.; Kang, K. Solvated ion intercalation in graphite: Sodium and beyond. *Frontiers in Chemistry* **2020**, *8*, 8.

(7) Fan, L.; Li, X. Recent advances in effective protection of sodium metal anode. *Nano Energy* **2018**, *53*, 630.

(8) Hong, K.; Qie, L.; Zeng, R.; Yi, Z.; Zhang, W.; Wang, D.; Yin, W.; Wu, C.; Fan, Q.; Zhang, W.; Huang, Y. Biomass derived hard carbon used as a high performance anode material for sodium ion batteries. *Journal of Materials Chemistry A* **2014**, *2* (32), 12733.

(9) Xiao, B.; Rojo, T.; Li, X. Hard carbon as sodium-ion battery anodes: Progress and challenges. *ChemSusChem* **2019**, *12* (1), 133−144.

(10) Irisarri, E.; Ponrouch, A.; Palacín, M. R. Review—Hard carbon negative electrode materials for sodium-ion batteries. *J. Electrochem. Soc.* **2015**, *162* (14), A2476−A2482.

(11) Stevens, D.; Dahn, J. The mechanisms of lithium and sodium insertion in carbon materials. *J. Electrochem. Soc.* **2001**, *148* (8), A803.

(12) Qin, K.; Holguin, K.; Mohammadiroudbari, M.; Luo, C. A conjugated tetracarboxylate anode for stable and sustainable Na-ion batteries. *Chem. Commun.* **2021**, *57* (19), 2360−2363.

(13) Holguin, K.; Mohammadiroudbari, M.; Qin, K.; Luo, C. Organic electrode materials for non-aqueous, aqueous, and all-solid-state Na-ion batteries. *Journal of Materials Chemistry A* **2021**, *9* (35), 19083−19115.

(14) Huang, J.; Li, S.; Wang, Y.; Kim, E. Y.; Yang, Z.; Chen, D.; Cheng, L.; Luo, C. Spatial effect on the performance of carboxylate anode materials in Na-ion batteries. *Small* **2024**, *20*, 2308113.

(15) Shehab, M. K. K.; Weeraratne, S.; Huang, T. J.; Lao, K. U.; El-Kaderi, H. M. Exceptional sodium-ion storage by an aza-covalent organic framework for high energy and power density sodium-ion batteries. *ACS Appl. Mater. Interfaces* **2021**, *13* (13), 15083−15091.

(16) Luo, C.; Xu, G.-L.; Ji, X.; Hou, S.; Chen, L.; Wang, F.; Jiang, J.; Chen, Z.; Ren, Y.; Amine, K.; Wang, C. Reversible redox chemistry of azo compounds for sodium-ion batteries. *Angew. Chem., Int. Ed.* **2018**, *57* (11), 2879−2883.

(17) Luo, C. Organic electrode materials and carbon/small-sulfur composites for affordable, lightweight and sustainable batteries. *Chem. Commun.* **2023**, *59*, 9803−9817.

(18) Shea, J. J.; Luo, C. Organic electrode materials for metal ion batteries. *ACS Appl. Mater. Interfaces* **2020**, *12* (5), 5361−5380.

(19) Luo, C.; Shea, J. J.; Huang, J. A carboxylate group-based organic anode for sustainable and stable sodium ion batteries. *J. Power Sources* **2020**, *453*, 227904.

(20) Medabalmi, V.; Kuanr, N.; Ramanujam, K. Sodium naphthalene dicarboxylate anode material for inorganic-organic hybrid rechargeable sodium-ion batteries. *J. Electrochem. Soc.* **2018**, *165* (2), A175.

(21) Mohammadiroudbari, M.; Qin, K.; Luo, C. Multi-Functionalized Polymers as Organic Cathodes for Sustainable Sodium/Potassium-Ion Batteries. *Batteries & Supercaps* **2022**, *5* (6), No. e202200021.

(22) Fuhrer, T. J.; Houck, M.; Iacono, S. T. Fluoromaticity: The Molecular Orbital Contributions of Fluorine Substituents to the π-Systems of Aromatic Rings. *ACS omega* **2021**, *6* (48), 32607−32617.

(23) Tian, Z.; Zou, Y.; Liu, G.; Wang, Y.; Yin, J.; Ming, J.; Alshareef, H. N. Electrolyte solvation structure design for sodium ion batteries. *Advanced Science* **2022**, *9* (22), 2201207.

(24) Kim, K. C.; Liu, T.; Jung, K. H.; Lee, S. W.; Jang, S. S. Unveiled correlations between electron affinity and solvation in redox potential of quinone-based sodium-ion batteries. *Energy Storage Materials* **2019**, *19*, 242−250.

(25) Huang, J.; Callender, K. I.; Qin, K.; Girgis, M.; Paige, M.; Yang, Z.; Clayborne, A. Z.; Luo, C. Halogenated carboxylates as organic anodes for stable and sustainable sodium-ion batteries. *ACS Appl. Mater. Interfaces* **2022**, *14* (36), 40784−40792.

(26) Frisch, M. E.; Trucks, G.; Schlegel, H.; Scuseria, G.; Robb, M.; Cheeseman, J.; Scalmani, G.; Barone, V.; Petersson, G.; Nakatsuji, H. *Gaussian 16*, revision C.01; Gaussian, Inc.: Wallingford, CT, 2016

(27) Lee, C.; Yang, W.; Parr, R. G. Development of the Colle-Salvetti correlation-energy formula into a functional of the electron density. *Phys. Rev. B* **2016**, *37* (2), 785.

(28) Orio, M.; Pantazis, D. A.; Neese, F. Density functional theory. *Photosynthesis Research* **2009**, *102*, 443−453.

(29) Tirado-Rives, J.; Jorgensen, W. L. Performance of B3LYP density functional methods for a large set of organic molecules. *J. Chem. Theory Comput.* **2008**, *4* (2), 297−306.

(30) McGrath, M. P. On the 6-311G basis set of bromine. *J. Chem. Phys.* **2009**, *130* (17), 176101.

(31) Grimme, S.; Ehrlich, S.; Goerigk, L. Effect of the damping function in dispersion corrected density functional theory. *Journal of computational chemistry* **2011**, *32* (7), 1456−1465.

(32) Grimme, S.; Antony, J.; Ehrlich, S.; Krieg, H. A consistent and accurate ab initio parameterization of density functional dispersion correction (DFT-D) for the 94 elements H-Pu. *J. Chem. Phys.* **2010**, *132* (15), 154104.

(33) Ye, Z.; Xie, S.; Cao, Z.; Wang, L.; Xu, D.; Zhang, H.; Matz, J.; Dong, P.; Fang, H.; Shen, J.; Ye, M. High-rate aqueous zinc-organic battery achieved by lowering HOMO/LUMO of organic cathode. *Energy Storage Materials* **2021**, *37*, 378−386.

(34) Song, J.; Bazant, M. Z. Effects of nanoparticle geometry and size distribution on diffusion impedance of battery electrodes. *J. Electrochem. Soc.* **2013**, *160* (1), A15.

(35) Chrzescijanska, E.; Wudarska, E.; Kusmierek, E.; Rynkowski, J. Study of acetylsalicylic acid electroreduction behavior at platinum electrode. *J. Electroanal. Chem.* **2014**, *713*, 17−21.

https://doi.org/10.1021/acsaem.4c00664
ACS Appl. Energy Mater. XXXX, XXX, XXX−XXX